Reactive Transport Modeling and Sensitivity Analysis of Column Experiments on fate of Alkaline-Saline Tank Waste Solutions in Variably Saturated Media

Zuoping Zheng and Guoxiang Zhang

(Earth Science Division, Lawrence Berkeley National Laboratory, Berkeley, CA 94720)

Abstract

Leakage of the alkaline-saline tank waste solutions under the SX tank farm at the U.S. Department of Energy (DOE)'s Hanford site is a serious environmental contamination problem. To better understand the mechanisms controlling the fate of the tank waste solutions in the Hanford vadose zone, we performed reactive transport simulation incorporated within the Pitzer ion-interaction model. Principal geochemical reactions considered in the model include quartz dissolution, dissolution/precipitation of Calcite, Brucite, and Portlandite , multi-component cation exchange, and aqueous complexation reactions. The model results were compared with laboratory column experiments conducted at both room temperature (21±1^{o}C) and high temperature (70±1^{o}C). Modeled pH and main cations (including Ca^{+2} and Mg^{+2}) show good matches to the measured data at room temperature. The model slightly overpredicts pH at all times, but most significantly at early time, although relatively good agreement was obtained at high temperature for the main cations such as Ca^{+2} and Mg^{+2}. The decrease of pH in the plume front is examined through precipitation of Ca-Mg-containing secondary phases and/or quartz dissolution. Substantial formation of Ca-Mg-containing mineral phases resulting from multi-component cation exchange, and the good relationship with pH, suggest that these Ca-Mg-containing phases are responsible for changes in pH within the plume front. To assess influences of different processes on the fate of alkaline-saline tank waste solutions, we conducted a sensitivity analysis with respect to cation exchange capacity (CEC), selectivity coefficient (SC), mineral assemblage, temperature, column length, and ionic strength (IS). From this analysis, we found that the effect of CEC and SC on cations such as Ca^{+2}, Mg^{+2}, and K^{+} is approximately linear. Changes in pH within the plume front constrained by secondary Ca-

Mg-containing phases are a function of temperature. As expected, the effect of column length on cation concentration of Ca^{+2} and Mg^{+2} is fairly pronounced, with the peak concentrations of cations such as Ca^{+2}, Mg^{+2}, and K^{+} in the plume front (due to multi-component cation exchange) proportional to column distance. IS greatly influences both pH and concentrations of Ca^{+2}, Mg^{+2}, and K^{+}. The lower IS (~1M) decreases pH within the plume front and significantly decreases exchangeable cation concentration. The results indicate that intensive multi-component complexation, base-induced quartz dissolution, multiple-phase precipitation, and multi-component cation exchange occurred in the soil during reactive transport of alkaline-saline tank waste solutions. These inter-related processes result in pH neutralization, increased Ca-Mg-containing mineral precipitation, and enhanced Ca^{+2} and Mg^{+2} release within the plume front during transport of alkaline-saline waste solutions in subsurface environments.

Key words: Alkaline-saline tank waste solutions; Laboratory experiments; Sensitivity analysis; Reactive transport modeling; Pitzer Ion-Interaction; Hanford site

1. Introduction

Leakage of alkaline-saline tank waste solutions from underground storage tanks at DOE's Hanford site strongly impact subsurface environments (Riley et al., 1992; Serne et al., 2001). Over the last 40 years, 67 of the 149 single-shell tanks at the Hanford site have leaked, releasing over 1 million gallons of waste solutions to the vadose zone (Gephart and Lundgren, 1998). As a result, locally elevated contaminant concentrations have been found in the vadose zone and groundwater beneath the SX tank farm (Ward et al., 1997). There is a great environmental concern about contamination of the underlying vadose zone, aquifer, and ultimately the Columbia River resulting from these leaks and potential future leaks. Predicting the vulnerability of subsurface porous media to these tank waste solutions requires the understanding of coupled physical and chemical processes.

Over the past several years, a great deal of research has focused on either physical processes or specific geochemical reaction mechanisms responsible for migration of radioactive Cs^{+}. This research has included field monitoring, laboratory experiments, and modeling (Serne et al., 2001; Pruess et al., 2002; Freedman et al., 2003; Steefel et al.,

2003). For example, Serne et al.(2001) reported dramatically decreased pH values within tank waste plumes measured in borehole samples collected from underneath the single-shell tank SX-108. Bickmore et al.(2001) and Wan et al.(2002) studied the formation of secondary phases through waste fluid–sediments interactions. Pruess et al. (2002) investigated two-phase heat and mass flow in the vicinity of boiling tanks. Zachara et al. (2002) and Steefel et al. (2003) proposed two-site equilibrium ion-exchange and three-site ion-exchange model, respectively, to describe Cs^+ transport. More recent work includes the role of nonideality of the sorbed cations and temperature dependence of selectivity coefficients (Liu et al., 2004), neutralization of alkaline and saline solutions (Wan et al., 2004a), an overall geochemical evolution of the major cations within the tank waste plumes (Wan et al., 2004b), kinetic formation of sodium aluminum nitrate silicate hydrate (Chorover et al., 2003), and competitive cation exchange on chromatographic displacement of cesium (Lichtner et al., 2004). These studies, to varying degrees, have led to substantial and continuous improvement in our quantitative and qualitative understanding of the behavior of tank waste solutions released into the Hanford vadose zone. However, relatively few studies have been conducted on reactive transport of tank waste solutions. Hence, reactive transport within this environment remains poorly understood because of their interdependence and extreme disequilibrium, especially during the early stages of tank-waste solutions transport. On the other hand, given the extreme thermodynamic properties of tank waste solutions (e.g., high ionic strength (5M - 20M), high density and viscosity, strong caustic (pH above 10), and chemical reactivity (Agnew et al., 1996; Jones and Maclean, 2000), achieving a general understanding of coupled geochemical processes and their transport is even more challenging, because strong ion interaction occurs and processes are closely interrelated. Potential pH-dependent processes such as aqueous complexation, dissolution of silicate, and precipitation of secondary mineral phases, multi-component cation exchanges are expected to yield complex scenarios during subsurface transport of alkaline-saline solutions.

In this study, we use BIO-CORE$^{2D©}$ to conduct quantitative simulations of fate of alkaline-saline waste solutions in well-controlled laboratory column experiments. The objectives of this research are (1) to evaluate a conceptual model of reactive transport against a detailed dataset (effluent chemistry) obtained from laboratory column

experiments; (2) to conduct a sensitivity analysis of cation exchange capacity (CEC), selectivity coefficients, mineral assemblages, temperature, column length, and ionic strengths with respect to laboratory column experiments under room temperature conditions. The results show that the relevant multiple coupled processes (multi-component cation exchange and mineral dissolution/precipitation) predominantly control fate of tank waste solutions in subsurface environments.

2. Modeling Approach

2.1 Computer Code

To model the reactive transport of alkaline-saline waste solutions in subsurface environments, we attempted to use BIO-CORE$^{2D©}$ (Zhang and Samper, 2001), a reactive geochemical transport code incorporating a Pitzer-type ion-interaction module (Zhang et al., 2004). BIO-CORE$^{2D©}$ is a multi-component reactive transport code applicable to nonisothermal variable saturated porous media that was developed as a member of the CORE family of codes (Samper et al., 2000) at the University of La Coruña, Spain. Conservation equations for heat transfer, water flow, solute transport, and geochemical processes are sequentially coupled. The code uses a two-dimensional and axial symmetrical three-dimensional Galerkin finite-element method for spatial discretization. Chemical reactions in the code include homogeneous aqueous complexations, acid-base, redox, mineral dissolution/precipitation, and ion exchange and dissociation of H_2O involving either local-equilibrium or kinetic-reaction mechanisms. While BIO-CORE$^{2D©}$ includes a much broader set of capabilities, in this study, the model ensures a better taking into account of multi-component cation exchange, aqueous complexation, precipitation and dissolution, and advective and dispersive transport in a variably saturated soil, which are major processes responsible for the behavior of tank waste solutions in subsurface.

2.2 Model Setup and Parameters

Our simulations in this study were focused on a 25 cm column experiments operated under room and high temperatures, as described below. Geometric and flow and transport parameters used are shown in Table 1. The 25 cm column was discretized into 200 spaced triangle elements. Injection was equally applied to two end nodes representing the injection port with equal flow rate. The lateral boundaries were set to be impermeable.

A large number of parameters are involved in the modeling. In general, the parameters used are directly collected from experimental measurements and include pore flow velocity, porosity, and hydraulic conductivity (where available). When parameters are not experimentally accessible, reported literature values are selected, specifically for diffusion coefficient, surface areas, and van Genuchten parameters. Thermodynamic data were gathered from two attached BIO-CORE$^{2D©}$ databases in which most of the data are initially from EQ3/6 database (Wolery, 1992). Table 4 lists thermodynamic data of minerals considered in our study.

3. Experiments

3.1. Initial Conditions

The sediments used for column experiments are Hanford formation "coarse sand," which contains quartz, feldspar, and basaltic rock fragments with 93% sand, 6% silt, and 1% clay (Table 2) (Serne et al., 2001). The average grain density is 2.77 Mg/m^3. Calcite comprises 1.1% of the total mass. The clay-sized fraction is composed of 40% illite, 20% smectite, 20% mixed-layer illite and smectite, and 20% kaolinite, with trace amounts of chlorite. The pH, measured in a 1:1 w/w water extract, was 8.4 (Wan et al., 2004b). CEC reported for the Hanford sand varies from 7 meq/100 g to 12meq/100 g (Serne et al., 2001; Zachara et al., 2002; Steefel et al., 2003). A 7 meq/100g of CEC was used in our modeling.

A common feature of the tank waste solutions is high ionic strength (>1.0 mol/L), resulting from large amounts of NaOH and $NaNO_3$ (Serne et al., 2001). Because of the variability and complexity of tank waste's chemical composition, a synthetic solution was designed to mimic the chemical compositions of the tank waste, as shown in Table 3 (Wan et al., 2004b). The pH of the solution measured is approximately 14, and the ionic strength is approximately 8 mol/L.

The initial pore water compositions were estimated based on the interaction of main sediment phases (Table 2) with distilled water, but calibrated with some direct measurements.

3.2 Laboratory Column Experiments

An array of laboratory column experiments were conducted under room- and high-temperature conditions to investigate reactive transport of synthetic tank waste solutions

(Wan et al., 2004a,b). A detailed description of the column setup, preparation, and sampling methods for the column experiments was provided in Wan et al. (2004a). Briefly, A 25 cm length column with an identical inner diameter (3.8 cm) were used. The Hanford sediments with 6% mass initial moisture were packed into the columns, and a final bulk density of 1.65 Mg m^{-3} was obtained for the packed sediments. To prevent channeling and gravity-induced flow fingering, the initial synthetic tank waste solutions shown in Table 3 were injected upwards at a pore-water velocity of 10 cm d^{-1} from the bottom to the top of the vertical columns, where the effluent samples were collected. In this way, the columns were practically saturated after the first pore volume of injection. Similar column experiments were conducted at 70±1^{o}C in a sealed water bath. Changes in fluid parameters and influences on solute transport were believed to be small, because only a few pore volumes of the synthetic solutions were injected.

3.3 Conceptual Model

Primary mineral dissolution/precipitation reactions considered (Table 4) were based on previous scan electron microscopy and x-ray diffraction identification data of the effluent from the column experiments described in Wan et al. (2004b). The secondary phases identified were mostly Ca-Mg-containing minerals, such as calcite, dolomite, and Si-Al-containing phases (i.e., sodium meta-silicate, cancrinite, and diaspore). Some Ca-Mg-containing minerals such as portlandite and brucite were also included in the model, based on the equilibrium between injection solution and Hanford sediment (although these minerals were not reported on the experiments). In addition to mineral reactions noted above, experimental data showed a significant increase in Ca^{+2}, Mg^{+2}, and K^{+} concentrations in the front of the column experiments, indicating a rich source of Ca^{+2}, Mg^{+2}, and K^{+} within the column sediments. Multi-components cation exchange was thus assumed. The increase of Ca^{+2}, Mg^{+2}, and K^{+} concentration in the front was believed to result from multi-component cation exchange, since mineral sources available in the initial Hanford sediments were very limited for those elements. As stated earlier, Hanford sediment contains ~1% carbonate, which can dissolve in response to geochemical changes in the pore water, including changes in pH. Furthermore, under alkaline conditions, quartz dissolution is significantly enhanced (Langmuir, 1997). Based on our recent literature

review, we proposed an empirical rate expression of quartz dissolution, calibrated through our previous batch experiments (Wan et al., 2004a).

$$r(\text{mol of Si } s^{-1}) = (a_q k_q)[OH^-]^{0.3} \quad (1)$$

where r is the dissolution rate, a_q is the reactive quartz surface area, and k_q is the rate constant. In response to the higher surface area of quartz, quartz dissolution rate is supposed to increase. Dissolution/precipitation of all other phases, however, was assumed at equilibrium, because of the lack of appropriate kinetic data. In addition, the components and the relevant aqueous complexation considered in the model were based on the initial pore-water compositions shown in Table 3. To facilitate convergence and reduce CPU time, dominant species in the initial solution were chosen as primary species under alkaline conditions. Hence, in place of H^+, Al^{+3}, the species OH^-, and $Al(OH)_4^-$ were chosen as primary species. Mass action equations and kinetic reaction rates were then expressed in terms of these species. Debye-Huckel model and Pitzer model were used for activity coefficient calculations (Zhang et al., 2004).

4. Results and Discussion

4.1. pH and Dissolution/Precipitation of Mineral Phases

Modeled breakthrough curves for the effluent pH as well as precipitation of secondary mineral phases for column experiments at 21^{o}C are shown in Figure 1a. Column effluent pH initially starts at approximately 8.3 (pore water pH), gradually decreases to 6.5 and then increases quickly to around 14 over the rest of the experiments. Simulated pH shows a good fit to the column data where experimental data are available. The pH data from both model simulations and column experiments at 70 ^{o}C are shown in Figure 1b. The model slightly overpredicts pH at virtually all times, but overpredicts more significantly at early times, indicating some inconsistency in the model. The pH in the column system is controlled by a complex interaction between quartz dissolution, mineral precipitation, and the solution chemistry. The decrease in pH in the reaction front could be examined through analyzing spatial profiles of total component concentrations and precipitation of mineral phases at the same time.

The dominant precipitation phases consist of Ca-Mg-containing minerals such as portlandite, calcite, anhydrite, and brucite, as well as silicate minerals such as cancrinite

and sodium meta-silicate, as shown in Figure 1. Results from modeling showed that solutions became immediately supersaturated in columns at approximately 1.2 pore volume. Both anhydrite and sodium meta-silicate were formed only at 70 ^{o}C. In addition, the amount of all secondary phases formed at 70 ^{o}C is much higher than that at 21 ^{o}C. Precipitation of Ca-Mg-containing minerals including calcite, portlandite, and brucite reaches its maximum after a short time. This time is very close to the pH decrease point in the reaction front, reflecting a spatial relationship between mineral precipitation and pH. It is reasonable to believe that Ca-Mg-containing phases noted above are responsible for the pH decrease in the plume front. In addition, formation of dolomite and diaspore was minimal, and has a limited influence on pH. On the other hand, the solid phases in the simulations were used exclusively to interpret experimental data. Since no quantitative analysis of solid phases was done during the column experiments, the direct comparison at various times cannot be made. Previous studies indicated that minerals in the groups of zeolite and/or cancrinite were formed in Al and Na-rich hyperalkaline systems (Zheng et al., 1997; Barnes et al., 1999; Bickmore et al., 2001). A recent modeling study suggested that the transport-controlled precipitation of NO_3-cancrinite, brucite and gibbsite occurred in the sediments under alkaline and saline conditions (Qafoku et al., 2004). The extent of precipitation of silicate phases apparently depends on the availability of Si in the aqueous phase. These results are consistent to our modeling observations under different temperatures noted above. Compared to Figure 2, the peak locations of Ca-Mg-containing phases coincide with those of cations, reflecting their relationship, as discussed below.

4.2. Exchangeable Cations, Ca^{+2}, Mg^{+2}, and K^{+}

Modeled breakthrough curves of effluent pH as well as Ca^{+2}, Mg^{+2}, and K^{+} under room and high temperatures are shown in Figure 2. The injection of alkaline-saline solutions with high Na^{+} concentration resulted in substantial releases of Ca^{+2}, Mg^{+2}, and K^{+} from the sediments, which peaked at ~ 1.1 pore volume, then decreased in the plume front for both column experiments. These increases obviously result from rapid and completed multiple cation exchanges with respect to Na^{+}. Modeled Ca^{+2} and Mg^{+2} concentrations show a reasonable match to the measured data. Some discrepancies were also observed, because of a likely dilution influence. As indicated in Figure 2, the concentration peaks of Ca^{+2} and Mg^{+2} observed in the experiments are different for room and high temperatures.

This discrepancy probably results from the precipitation of secondary mineral phases considered. Although Ca-Mg-bearing minerals consume aqueous Ca^{+2}, Mg^{+2}, and carbonate, Ca^{+2} and Mg^{+2} are still predominant in aqueous form. In addition, the temperature-dependent selectivity coefficients (Liu et al., 2003; Lichtner et al., 2004) were recently reported and could, to a certain degree, influence exchangeable cation concentrations.

The peak of exchangeable cations such as Ca^{+2}, Mg^{+2}, and K^{+} observed in the plume front is proportional to their cation fractions in the sediment. The behavior of Ca^{+2} and Mg^{+2} in solution is related to the change in competition for surface sites and speciation. As reported in the literature (e.g., Appelo and Postma, 1996; Bashir et al., 2002), adsorbent (such as clay minerals) normally have a stronger affinity for Ca^{+2} and Mg^{+2} than Na^{+}. However, an extreme high concentration of Na^{+} in the infuse solution (8 mol L^{-1}) considerably enhances its affinity to soil absorbents. This is confirmed with other experiments (Bashir et al., 2002). Greater selectivity coefficients can be obtained through the inclusion of solute interactions within the system, depending upon solution chemistry such as pH, ionic strength and temperature (Bashir et al., 2002). On the other hand, both OH^{-} and CO_3^{2-} ligands might be important complexants within alkaline waste solutions at elevated ionic strength such that both ligands complex Ca^{+2} and Mg^{+2} more strongly than Na^{+} based on their chemistry properties (Appelo and Postma, 1996; Felmy et al., 1998a,b). The peak of Ca^{+2} and Mg^{+2} appear to depend on their different initial fractions in soil sediments, owing to the use of the same selectivity coefficients. As shown in Table 3, Ca^{+2} and Mg^{+2} exchange fractions in soils at equilibrium with pore-water is approximately 80% and 20% , respectively.

A salinity front dominated by $NaNO_3$ (the primary electrolyte in the Hanford tank leaks) moves through Ca and Mg-bearing sediments. The extremely high Na^{+} concentrations in the waste solutions brought about a rapid and complete cation exchange, resulting in concentration peaks of Ca^{+2} and Mg^{+2} at the plume front. Ca^{+2} and Mg^{+2} quantities in the plume front are within the range expected, but also consumed by precipitation of secondary minerals such as calcite, portlandite, brucite, and /or anhydrite. The net result is the mutual enhancement of the two processes, resulting in increased calcite and brucite precipitation, enhanced dissolved Ca^{+2} and Mg^{+2} concentration, and pH

neutralization of alkaline solutions. As shown in Figure 2, the precipitation of calcite and brucite ceases as the Ca^{+2} and Mg^{+2} concentrations approach pore-water level (~10^{-4}M).

Although simulations presented in Figure 1 and 2 were unable to exactly reproduce the observed data, the general agreement, in particular the decrease of pH within the plume front, would tend to indicate that the conceptual model used is a reasonable representation of the geochemical system in the column. It is difficult to state with certainty that the model parameters and conceptual model presented here are unique. In fact, the discrepancy noted in the simulated and observed effluent pH and cation concentrations of Ca^{+2}, Mg^{+2}, and K^{+} indicate that the model as presented may be incomplete. However, the principal modeling results reasonably capture the results from the column experiments.

5. Sensitivity Analysis

A sensitivity analysis of CEC, selectivity coefficients (SC), mineral assemblage, temperature, column length, and ionic strength (IS) was performed to assess the role of each geochemical parameters and processes in subsurface reactive transport of alkaline-saline tank waste solutions. The one-dimensional simulation of column experiment at 21 ^{o}C presented in Figure 1 and 2 was served as the reference case for comparison. Simulation results of the sensitivity analysis with respect to change in each parameter or process were compared based on (1) the maximum exchangeable cation concentration (MECC) of Ca^{+2}, Mg^{+2}, and K^{+}, and (2) the decline of pH in the plume front.

5.1. CEC

In our modeling, it is assumed that CEC values remain unchanged over the entire simulation period. In fact, the CEC of soil may change depending on soil properties (clay content and particle size). The effect of CEC on reactive transport of tank waste solutions has been evaluated for the Hanford soil (Serne et al., 2001).

Breakthrough curves for modeled pH are almost identical for the soil sediments with different CEC values, because the precipitation/dissolution phases (calcite, cancrinite and quartz), which are supposed to govern pH, are quite similar, as shown in Table 5. Precipitation of portlandite, anhydrite, and brucite does not influence pH decrease within the plume front, because their maximum precipitation amount increases with CEC.

The MECC values for soil sediments with different CEC values are shown in Figure 3b. A linear trend is obtained for CEC values. However, marked changes exceeding the linear trend were observed, suggesting a secondary influence on MECC values in the system (although Figure 3b exhibits that MECC values of Ca^{+2}, Mg^{+2}, and K^{+} are, to different degrees, proportionally related to the initial CEC values). The MECC values of Ca^{+2}, Mg^{+2}, and K^{+} range from 0.6, 0.15, 0.032M to around 1.0, 0.2, 0.05M, as CEC increases from 7 to 12 meq/100 g, respectively. Obviously, these concentrations are closely related to the dissolution and precipitation, as discussed earlier.

The modeling results show that changes in CEC values have no noticeable influence on pH, but have a significant influence on MECC values and amounts of Ca-Mg-containing phases including calcite, brucite, and dolomite.

5.2. Selectivity Coefficients (SC)

Previous studies demonstrate that SC values for Cs^{+} exchange on illite and sediment observed varied by factors of 10 or more with changing electrolyte concentration (Zachara et al., 2002). It has been well documented that SC influences concentration and distribution of exchangeable cations. Different SC values for the couples Ca^{+2}-H^{+}, Mg^{+2}-H^{+}, and K^{+}-H^{+} are shown in Table 6. Other modeling parameters were remained the same.

Similar trends of changes in modeled pH in response to different SC values were observed, since maximal precipitation/dissolution of minerals are fairly consistent (Table 7). The MECC values of Ca^{+2}, Mg^{+2}, and K^{+} correspond well to different SC, as presented in Figure 4.

5.3. Minerals/Cation Exchange

The effect of mineral assemblages on reactive transport of tank waste solutions was analyzed in the absence and presence of multi-component cation exchange. Without considering quartz dissolution and mineral dissolution/precipitation, breakthrough curves of main cations (Figure 5), are much different from those shown in Figure 2. Although aqueous Ca^{+2} distribution and maximal concentration are comparable, Mg^{+2} distribution are very different without mineral constraint. Furthermore, consistent pH was observed within the plume front without mineral precipitatin/dissolution. Therefore, a decrease in pH at around 1.2 pore volumes is because of mineral precipitation, in particular Ca-Mg-bearing phases, as addressed previously.

To assess influences of quartz dissolution on pH, its rate was increased through increasing specific surface area, while other modeling parameters are remained the same as before. As shown in Figure 6, almost identical breakthrough curves were obtained as quartz dissolution rate changes, indicating that quartz dissolution slightly influences pH in the plume front.

5.4. Temperature

As a result of radioactivity, a large amount of the heat is supposed to be incorporated in the waste solutions, leading to an increase of the solution temperatures. The temperature range considered here are from 21 ^{o}C to 70 ^{o}C, representative of a field temperature range at the DOE Hanford site (Serne et al., 2001). How temperature affects SC, mineral dissolution/precipitation in alkaine-saline solutions is still largely unknown. It is useful, however, to perform numerical calculations with an elevated temperature, to assess the relevance of the basic assumptions in the geochemical model, that all temperatures are considered as constant.

Figure 7a and 7b present breakthrough curves for modeled pH with increasing temperature in the presence and absence of cation exchange, respectively. The pH difference is pronounced, in particular within the plume front. In the absence of cation exchange in the model, a significant decrease in pH within the plume front (Figure 7a) does not occur. In contrast, a marked decrease in pH within the plume front occurs in the presence of cation exchange (Figure 7b). These mechanisms could be interpreted from the precipitation of secondary mineral phases as, shown in Figure 8. The precipitation quantity of secondary mineral phases for calcite, portlandite, brucite, and anhydrite is enhanced with temperature in the presence of cation exchange. However, precipitation of secondary mineral phases is relatively low (dashed lines) and in general shows decreasing with temperature in the absence of cation exchange. It is clear that precipitation of Ca-Mg-containing minerals governs changes in pH within the plume front as temperature increases. Note that quartz dissolution and the related formation of secondary minerals such as cancrinite and sodium meta-silicate are equally accelerated for both cases with temperature (data not shown), indicating that a decrease in pH within the plume front is caused by cation exchange and precipitation of Ca-Mg-containing minerals.

The effect of temperature on the MECC values of Ca^{+2}, Mg^{+2}, and K^{+} is given in Table 8. The variations in their concentrations are relatively slight as a function of temperature, indicating that CEC and SC are still more important parameters than temperature. The simulated MECC values of Ca^{+2}, Mg^{+2}, and K^{+} are the same as the initial pore-water concentration level in the absence of cation exchange (data not shown).

5.5. Column Length

Previous laboratory experiments have demonstrated that column length is an important factor in subsurface affecting reactive transport of tank waste solutions (Wan et al., 2004b). In this study, modeling was therefore conducted with varying column lengths, while the rest of the setup remained the same as before. Breakthrough curves for pH in response to different column lengths are shown in Figure 9. Similar curves of pH are observed when the column length was standardized with respect to length, since quartz dissolution and precipitation of secondary minerals are similar (Table 9a). However, precipitation of Si-containing cancrinite is different, revealing a significant time dependency. The MECC values of Ca^{+2}, Mg^{+2}, and K^{+} are enhanced with increasing column length (Table 9a). As demonstrated in Figure 3b, the MECC values of Ca^{+2}, Mg^{+2} and K^{+} are proportional to the total CEC of soil sediments. Given the same soils used in the column, it is expected that total exchangeable cation fraction would be increased as column length increases. When column length is doubled, however, the MECC values increase only 70%, suggesting a mineral precipitation control on their concentration. The precipitation of secondary minerals consumes exchangeable cations, and thus decreases aqueous exchangeable cation concentrations.

5.6. Ionic Strength

High-ionic-strength solutions, in particular high Na^{+} concentrations, have been shown to significantly reduce Cs sorption to Hanford sediments (Flury et al., 2002; Zachara et al., 2002). The experiments presented in Wan et al. (2004a) also show that ionic strength strongly influences pH neutralization of alkaline-saline waste solutions. The tailing of pH breakthrough was observed at low ionic strength, but pronounced tailing also occurred at high ionic strength (Wan et al., 2004a). Detailed description of the experiments was presented in Wan et al. (2004a).

The main chemical components injected are NaOH and $NaNO_3$. The concentration of NaOH is set to 1M, with $NaNO_3$ is variable and used for adjusting ionic strength. The ionic strength range tested is from 1M to 8M. The mineral phases considered are therefore simplified, including only Ca-Mg-containing phases such as calcite, dolomite, portlandite, and dolomite. Breakthrough curves for modeled and effluent pH are presented in Figure 10 as different ionic strength solutions were infused into the column. The modeling results are generally comparable to the experimental data, although some discrepancies were observed for an ionic strength of 3M. In addition, pH tailing was also observed in ionic strength solutions of 1 M and 8 M. The effect of ionic strength on formation of secondary minerals is complex. Precipitation of dolomite is enhanced by increasing ionic strength, likely affecting changes in pH within the plume front. The effect of ionic strength on exchangeable cation Ca^{+2}, Mg^{+2}, K^{+} was considerable, as presented in Table 10b. In general, MECC values of Ca^{+2}, Mg^{+2}, and K^{+} are highly enhanced as ionic strength increased from 1 to 8 M.

The results from sensitivity analysis indicate that CEC, SC, and column length significantly influence MECC values, but not pH. However, mineral assemblages in particular formation of Ca-Mg-containing minerals, strongly control changes in pH within the plume front. Temperature and ionic strength are important factors affecting pH, MECC values, and formation of secondary minerals.

6. Conclusions

Incorporating the Pitzer ion-interaction module into the framework of a reactive transport code BIO-CORE$^{2D©}$ has enabled to simulate of the geochemical evolution of alkaline-saline waste solutions at elevated ionic strength.

The proposed geochemical model was validated by comparison to laboratory column experiments. The results indicated that multi-component cation exchange, quartz dissolution, and multiple formation of secondary phases (including calcite, portlandite, brucite, and cancrinite) together control the fate of tank waste solutions, leading to a decrease in pH within the plume front. Laboratory column experiments validate the capability of the model to capture realistic field observations. This study should serve as a

useful guide both to subsequent experimental work and to thermodynamic models developed for concentrated solutions at high ionic strength.

The physico-chemical processes considered in the model were further investigated through sensitivity analyses with respect to CEC, SC, temperature, column length, and IS. These parameters, to varying degrees, influence the fate of tank waste solutions in the subsurface. Accurate determination of individual parameters and identification of different mineral phases are needed to understand movement of tank waste solutions.

The fate of tank waste solutions in the vadose zone is closely related to the extent of multi-component cation exchange, multiple-phases dissolution/precipitation, and multi-component ionic interaction. The resulting changes in the aqueous chemistry such as pH, Ca, Mg, K, and Si and solid phases such as formation cancrinite, calcite, burcite, and portlandite are anticipated to affect the behavior of radionuclide (adsorption, reactivity, and transport) in subsurface environments.

Acknowledgements

This work was carried out under U.S. Department of Energy Contract No. DE-AC03-76SF-00098. This research was supported by the Basic Energy Science Program of the Office of Science, U.S. Department of Energy. The authors thank Tianfu Xu (LBNL) and Daniel Hawkes (LBNL) for an internal review.

References

Appelo, C.A.J., Postma, D., 1996. Geochemistry, Groundwater and Pollution. A.A. Balkema, Rotterdam.

Agnew, S. F., Boyer, J., Corbin, R. A., Duran, T. B., Fitzpatrick, J. R., Jurgensen, K. A., Ortiz, T. P., and Young, B. L. 1996. Hanford tank chemical and radionuclide inventories: HDW Model, LA-UR-96-858, Los Alamos National Laboratory, Los Alamos, NM.

Barnes, M.C., Addai-Mensah, J., Gerson, A.R., 1999. The mechanism of the sodalite-to-cancrinite phase transformation in the synthetic spent Bayer liquor. Microporous Mater. 31, 287-302.

Bashir, W., Tyrrell, E., Feeney, O., Paull, B., 2002. Retention of alkali, alkaline earth and transition metals on an itaconic acid cation exchange column eluent pH, ionic strength

and temperature effects upon selectivity. J. Chromatography A, 964, 113-122.

Bickmore, B.R., Nagy, K.L., Young, J.S., Drexler, J.W., 2001. Nitrate-cancrinite precipitation on quartz sand in simulated Hanford tank solutions, Environmental Science Technology 35, 4481-4486.

Chorover, J.; Choi, S.; Amistadi, M.K.; Karthikeyan, K.G.; Crosson, G.; Mueller, K.T., 2003. Linking cesium and strontium uptake to kaolinite weathering in simulated tank waste leachate. Environmental Science and Technology, 37, 2200-2208.

Felmy, A.R., Dixon, D.A., Rustad, J.R., Mason, M.J., Onishi, L.M., 1998a. The hydrolysis and carbonate complexation of strontium and calcium in aqueous solution. Use of molecular modeling calculations in the development of aqueous thermodynamic models. Journal of Chemical Thermodynamics 30, 1103-1120.

Felmy, A.R., Mason, M.J., 1998b. The Displacement of Sr from organic chelates by hydroxide, carbonate,and cacium in concentrated electrolytes. Journal of Solution Chemistry 27, 435-454.

Flury, M., Mathison, J.B., Harsh, J.B., 2002. In situ mobilization of colloids and transport of cesium in Hanford sediments. Environmental Science and Technology, 36, 5335-5341.

Freedman, V.L., Saripalli, K.P., Meyer, P.D., 2003. Influence of mineral precipitation and dissolution on hydrologic properties of porous media in static and dynamic systems. Applied Geochemistry 18, 589-606.

van Genuchten, M.T., 1980. A closed-form equation for predicting the hydrauluc conductivity of unsaturated soils. Soil Science Society American Journal 44, 892-898.

Gephart,R.E., Lundgren, R.E., 1998. *Hanford Tank Cleanup*, Battelle, Columbus, OH.

Johnston, C.T., Agnew, S.F., Schoonover, J.R., Kenney, J.W., Page, B., Osborn, J., Corbin, R., 2002. Raman study of aluminum speciation in simulated alkaline nuclear waste. Environmental Science and Technology 36, 2451-2458.

Jones, T. E., and Maclean, G. T., 2000. Inventory estimates for single-shell tank leaks in S and SX tank farms, RPP-6285, CH2MHILL Hanford Group, Inc., Richland, Washington.

Langmuir, D. 1997. Aqueous Environmental Geochemistry. Upper Saddle River, N.J. Prentice Hall. 1997

Lichtner, P.C.; Yabusaki, S.; Pruess, K.; Steefel, C.I. 2004. Role of competitive cation exchange on chromatographic displacement of cesium in the vadose zone beneath the

Hanford S/SX tank farm. Vadose Zone J. 3: 203-219.

Liu, C.; Zachara, J.M.; Qafoku, O.; Smith, S.C. 2003. Effect of temperature on Cs+ sorption and desorption in subsurface sediments at the Hanford site, U.S.A. Environmental Science and Technology, 37, 2640-2645.

Mualem, Y., 1976. A new model for predicting the hydraulic conductivity of unsaturated porous media. Water Resources Research 12, 513-522.

Pruess, K., Yabusaki, S., Steefel, C., Lichtner, P., 2002. Fluid flow, heat transfer, and solute transport at nuclear waste storage tanks in the Hanford vadose zone. Vadoze Journal 1, 68-88.

Qafoku, N.P., Ainsworth, C.C., Szecsody, J.E., Qafoku, O.S., 2004. Transport-controlled kinetics of dissolution and precipitation in the sediments under alkaline and saline conditions. Geochim Cosmochim. Acta, 68, 2981-2995.

Riley, R. G., Zachara, J. M., and Wobber, F. J.,1992. Chemical contaminants on DOE lands and selection of contaminant mixtures for subsurface science research, DOE Office of Energy Research Subsurface Science Program, DOE/ER-0547T.

Samper, J., R., Juncosa, J. Delgado, and L. Montenegro, CORE^{2D}: A code for non-isothermal water flow and reactive solute transport. Users manual version 2. ENRESA Technical Publication 06/2000. 131 pp, 2000.

Serne, R.J., Schaef, H.T., Bjornstad, B.N., Lanigan, D.C., Gee, G.W., Lindenmeier, C.W., Clayton, R.E., LeGore, V.L., O'Hara, M.J., Brown, C.F., Orr, R.D., Last, G.V., Kutnyakov, I.V., Burke, D.B., Wilson, T.C., Williams, B.A., 2001. Geologic and Geochemical data collected from vadose zone sediments from borehole 299 W23-19(SX-115) in the S/SX waste Management Area and Preliminary Interpretations. PNNL-2001-3, Pacfic Northwest National laboratory, Richland, WA.

Steefel, C.I., Carroll, S., Zhao, P., Roberts, S., 2003. Cesium migration in Hanford sediment: a multisite cation exchange model based on laboratory transport experiments. Journal of Contaminant Hydrology.

Ward, A.L., Gee, G.W., White, M.D., 1997. A comprehensive analysis of contaminant transport in the vadose zone beneath tank SX-109. Pacific Northwest National Laboratory Report PNNL-11463, Richland, WA.

Wan, J., Tokunaga, T.K., Saiz, E., Olson, K.R., Larsen, J.T., 2002. Colloid formation

resulting from highly alkaline and saline waste tank solution leaking into sediments at the Hanford site. Lawrence Berkeley National Laboratory.

Wan, J, Larsen, J. T., Tokunaga, T. K., and Zheng, Z., 2004a. pH neutralization and zonation in alkaline-saline tank waste plumes, Environmental Science and Technology, *38*; 1321-1329.

Wan, J., Tokunaga, T.K., Larsen, J.T., Couture, R.A., 2004b. Geochemical evolution of highly alkaline and saline tank waste plumes during seepage through vadose zone sediments. Geochim Cosmochim Acta., 68, 491-502.

Wolery T. J. (1992) EQ3NR, A Computer Program for Geochemical Aqueous Speciation-Solubility Calculations: Theoretical Manual, User's Guide, and Related Documentation (Version 7.0) *Lawrence Livermore National Laboratory*,

Zachara, J.A., Smith, S.C., Liu, C., McKinley, J.P., Serne, R.J., Gassman, P.L., 2002. Sorption of Cs^+ to micaceous subsurface sediments from the Hanford site, USA, Geochim Cosmochim Acta 66, 193-211.

Zhang, G., Samper, J., 2001. BIO-CORE$^{2D©}$, a code for water flow and reactive transport including surface microbial processes-User's Manual, technique report, University of La Coruña, Spain

Zhang, G., Zheng, Z., Wan, J., Tokunaga, T.K., 2004. Modeling reactive geochemical transport of concentrated aqueous solutions in variably saturated media. Submitted to Water Resources Research.

Zheng, K., Gerson, A.R., Addai-Mensah, J., Smart, R.S.C., 1997. The influence of sodium carbonate on sodium aluminosilicate crystallization and solubility in sodium aluminate solutions. J. Cryst. Growth 171, 197-208.

Table Captions

Table 1. Physical Parameters Used in the Model

Table 2. Mineral Compositions of the Hanford Coarse Sand

Table 3. Compositions of the Solutions Used in Column Experiments (from Wan et al., 2004b)

Table 4. Reaction Stoichiometries for Mineral Precipitation/Dissolution Reactions

Table 5. The Maximal Precipitation of Mineral Phases in Response to Changes in CEC

Table 6. Selectivity Coefficients Used for the Sensitivity Analysis

Table 7. The Maximal Precipitation of Mineral Phases with Varying Selectivity Coefficients (M)

Table 8. The Maximal Exchangeable Cation Concentration and Aqueous Silica with Varying Temperatures

Table 9a. The Maximal Precipitation of Mineral Phases with Varying Column Lengths (M)

Table 9b. The Maximal Exchangeable Cation Concentrations with Varying Column Lengths (M)

Table 10a. The Maximal Precipitation of Mineral Phases with Varying Ionic Strength Solutions (M)

Table 10b. The Maximal Exchangeable Cation Concentration with Varying Ionic Strength Solutions (M)

Figure Captions

Figure 1. Breakthrough Curves for pH and Precipitation of Secondary Mineral Phases for 25 cm Tall Columns at 21 and 70 ^{o}C, respectively.
The lines denoted simulated results, whereas dispersed dots are experimental data.

Figure 2. Breakthrough Curves for pH and Exchangeable Cations Ca, Mg, and K for 25 cm Tall Columns at 21 and 70 ^{o}C, respectively.
The lines denoted simulated results, whereas dispersed dots are experimental data.

Figure 3. Breakthrough Curves for pH(a) and the Maximal Exchangeable Cation Concentration of Ca, Mg, and K (b) with varying CEC values.

Figure 4. The Maximal Exchangeable Cation Concentration of Ca, Mg, and K with Varying Selectivity Coefficients.

Figure 5. Breakthrough Curves for pH and Exchangeable Cations in the Absence of Mineral Dissolution/Precipitation at 21 ^{o}C.

Figure 6. Breakthrough Curves for pH with Varying Surface Area of Quartz in the Modeling System at 21 ^{o}C.

Figure 7. Breakthrough Curves for pH with Varying Temperatures in the Absence (a) or Presence (b) of Multi-component Cation Exchange.

Figure 8. The Maximal Precipitation of Secondary Phases with Varying Temperatures in the Absence (dashed lines) and Presence (solid lines) of Multi-component Cation Exchange.

Figure 9. Breakthrough Curves for pH with Varying Column Lengths at 21 ^{o}C.

Figure 10. Breakthrough Curves for Modeled pH (solid lines) and Measured pH (dots) with Varying Ionic Strength Injection Solutions for 25 cm Tall Columns at 21 ^{o}C.

Table 1

Parameter	Definition
Column	0.25 m (length) × 0.038 m (diameter) spatial discretization Δx= 0.0025 m
Flow	Flow rate = 0.0432 L/day; permeability = 0.64 m/day; Van Genuchten m = 0.731, α = 0.9 m.
Transport	Diffusion coefficient $D_0 = 10^{-9}$ m^2/s; dispersivity α_L = 0.002m Porosity 0.4

Table 2

	Percent %	Major Mineral	Percent %	Clay minerals in clay fraction	Percent %
Sand	87.4	Quartz	55	Illite	40
Silt	10.3	K-feldspar	30	Smectite	20
Clay	2.3	Na-feldspar	15	Mixed-layer illite and smectite	20
				Kaolinite	20

Table 3

Feeding solutions	Conc. (M)	Pore water	Conc. (mM)
Al	0.805	Na^+	1.088
CO_3^{--}	0.168	K^+	0.215
OH^-	1.47	Mg^{++}	0.181
NO_3^-	5.565	Ca^{++}	0.382
SO_4^{--}	0.06	Cl^-	0.27
Na^+	8.05	SO_4^{--}	0.56
SiO_2	0.0015	CO_3^{--}+HCO_3^-	1.29
pH	14.1	pH	8.4

Conc. : Concentration

Table 4

Reactions	Log K 21 °C	LogK 70 °C
SiO_2 (Quartz) $\rightarrow$ SiO_2(aq)	-4.09	-3.35
$AlO(OH) + 3H^+ \rightarrow Al^{+3} + 2H_2O$	-14.7	-13.0
$CaCO_3 + H^+ \rightarrow Ca^{+2} + HCO_3^-$	1.99	1.34
$CaMg(HCO_3)_2 + 2H^+ \rightarrow Ca^{+2} + Mg^{+2} + 2HCO_3^-$	2.67	1.00
$Ca(OH)_2 + 2H^+ \rightarrow Ca^{+2} + 2H_2O$	22.9	19.6
$CaSO_4 \rightarrow Ca^{+2} + SO_4^{-2}$	-4.26	-4.91
$Na_2SiO_3 + 2H^+ \rightarrow SiO_2(aq) + 2Na^+ + H_2O$	21	18.7
$Na_8(AiSiO_4)_6.2NO_3 + 12OH^- + 8H_2O \rightarrow 8Na^+ + 6Al(OH)_4^- + 6H_2SiO_4^{-2} + 2NO_3^-$	-53.5	-61.8
$Mg(OH)_2 + 2H^+ \rightarrow Mg^{+2} + 2H_2O$	16.6	13.8

All reactions are written in terms of the components used in the model.

Table 5

CEC (meq/100g)	Quartz (M)	Calcite (M)	Dolomite (M)	Portlandite (M)	Anhydrite (M)	Cancrinite (M)	Brucite (M)
7	-1.73E-02	5.48E-02	8.20E-05	6.10E-02	0.00E+00	2.20E-03	6.18E-02
8	-1.72E-02	5.56E-02	8.65E-05	6.20E-02	0.00E+00	2.18E-03	6.87E-02
9	-1.80E-02	5.85E-02	9.81E-05	7.29E-02	6.05E-04	2.29E-03	7.23E-02
10	-1.79E-02	5.85E-02	8.68E-05	7.30E-02	6.58E-03	2.29E-03	7.88E-02
11	-1.78E-02	5.85E-02	1.03E-04	7.30E-02	1.35E-02	2.29E-03	8.45E-02
12	-1.77E-02	5.79E-02	9.36E-05	7.23E-02	1.93E-02	2.28E-03	9.08E-02

Note: Negative means dissolution; positive refers precipitation

Table 6

Cation Exchange Reactions	SC1	SC2	SC3	SC4	SC5	SC6
$H^+ + NaX \rightarrow H\text{-}X + Na^+$	1	1	1	1	1	1
$H^+ + KX \rightarrow H\text{-}X + K^+$	0.8	0.9	0.6	0.5	0.3	0.3
$H^+ + 1/2CaX_2 \rightarrow H\text{-}X + 1/2Ca^{+2}$	0.5	0.6	0.3	0.2	0.6	0.2
$H^+ + 1/2MgX_2 \rightarrow H\text{-}X + 1/2Mg^{+2}$	0.4	0.5	0.2	0.1	0.7	0.4

Table 7

	Quartz (M)	Calcite (M)	Dolomite (M)	Portlandite (M)	Cancrinite (M)	Brucite (M)
SC1	-1.81E-02	5.94E-02	8.44E-05	7.31E-02	2.31E-03	6.11E-02
SC2	-1.81E-02	6.25E-02	8.40E-05	7.81E-02	2.31E-03	5.95E-02
SC3	-1.81E-02	5.56E-02	8.71E-05	6.84E-02	2.30E-03	6.01E-02
SC4	-1.52E-02	3.66E-02	6.83E-05	3.96E-02	1.92E-03	4.24E-02
SC5	-1.80E-02	3.19E-02	2.17E-04	3.46E-02	2.31E-03	1.35E-01
SC6	-1.80E-02	3.40E-02	1.39E-04	3.75E-02	2.31E-03	1.02E-01

SC: Selectivity Coefficients

Table 8

T (^oC)	Ca^{+2} (M)	Mg^{+2} (M)	Na^+ (M)	K^+ (M)	SiO_2(aq) (M)
21	6.83E-01	1.58E-01	8.02E+00	3.31E-02	3.78E-03
30	6.53E-01	1.69E-01	8.10E+00	3.19E-02	1.33E-03
40	6.28E-01	1.64E-01	8.16E+00	3.07E-02	3.33E-03
50	6.41E-01	1.46E-01	8.23E+00	3.10E-02	8.71E-03
60	6.49E-01	1.44E-01	8.24E+00	2.87E-02	2.38E-02
70	6.63E-01	1.32E-01	8.41E+00	2.85E-02	5.18E-02

Table 9a

CL (cm)	Quartz	Calcite	Dolomite	Portlandite	Cancrinite	Brucite
25	-1.52E-02	3.76E-02	7.04E-05	4.14E-02	1.92E-03	4.44E-02
15	-1.61E-02	5.06E-02	6.80E-05	5.52E-02	6.45E-04	5.32E-02
5	-1.54E-02	4.53E-02	5.84E-05	4.72E-02	0.00E+00	3.51E-02

Table 9b

CL (cm)	Na^{+} (M)	Ca^{+2} (M)	Mg^{+2} (M)	K^{+} (M)
25	8.02E+00	6.83E-01	1.58E-01	3.31E-02
15	8.05E+00	4.91E-01	1.15E-01	2.83E-02
5	8.05E+00	3.07E-01	6.42E-02	1.97E-02

Table 10a

IS (M)	Quartz (M)	Dolomite (M)	Portlandite (M)	Brucite (M)
1	-8.81E-03	8.62E-05	2.93E-02	1.52E-02
3	-5.38E-03	1.02E-04	0.00E+00	2.94E-03
5	-1.40E-02	1.39E-04	2.11E-02	4.86E-02
8	-5.35E-03	6.41E-04	0.00E+00	1.29E-02

Table 10b

IS(M)	Na^{+} (M)	Ca^{+2} (M)	Mg^{+2} (M)	K^{+} (M)
1	1.01E+00	2.93E-01	1.13E-01	7.05E-03
3	3.01E+00	6.71E-01	2.51E-01	2.32E-02
5	5.63E+00	8.36E-01	2.03E-01	3.21E-02
8	8.02E+00	8.65E-01	2.98E-01	3.05E-02

Figure 1

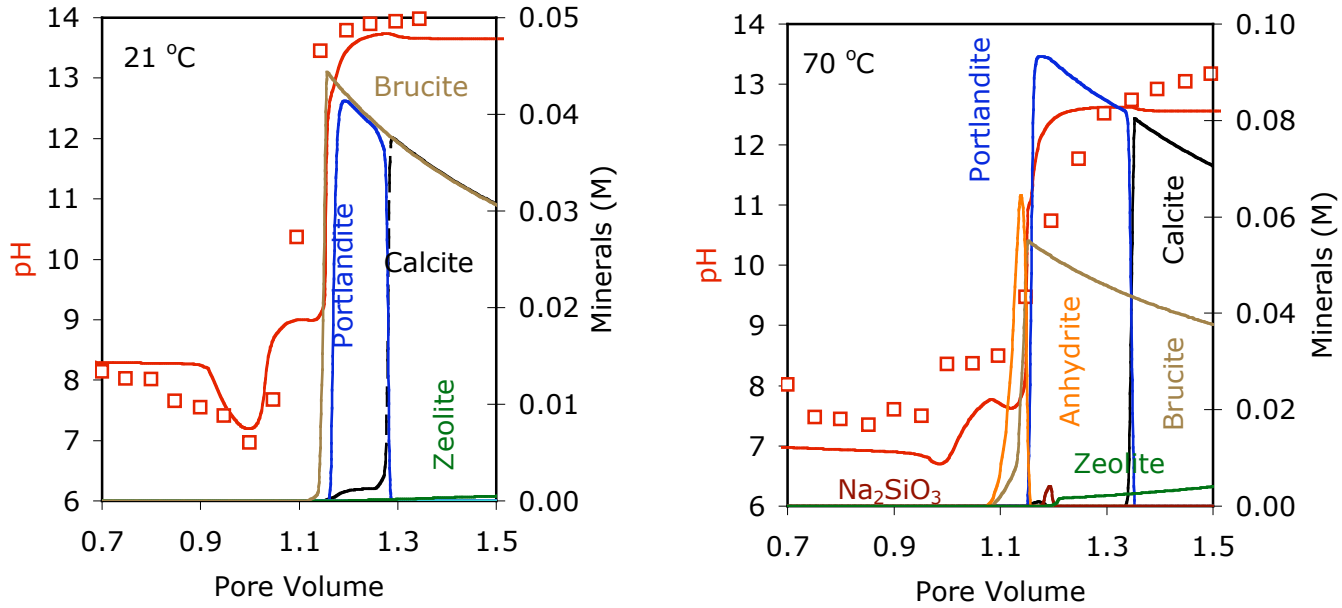

Figure 2

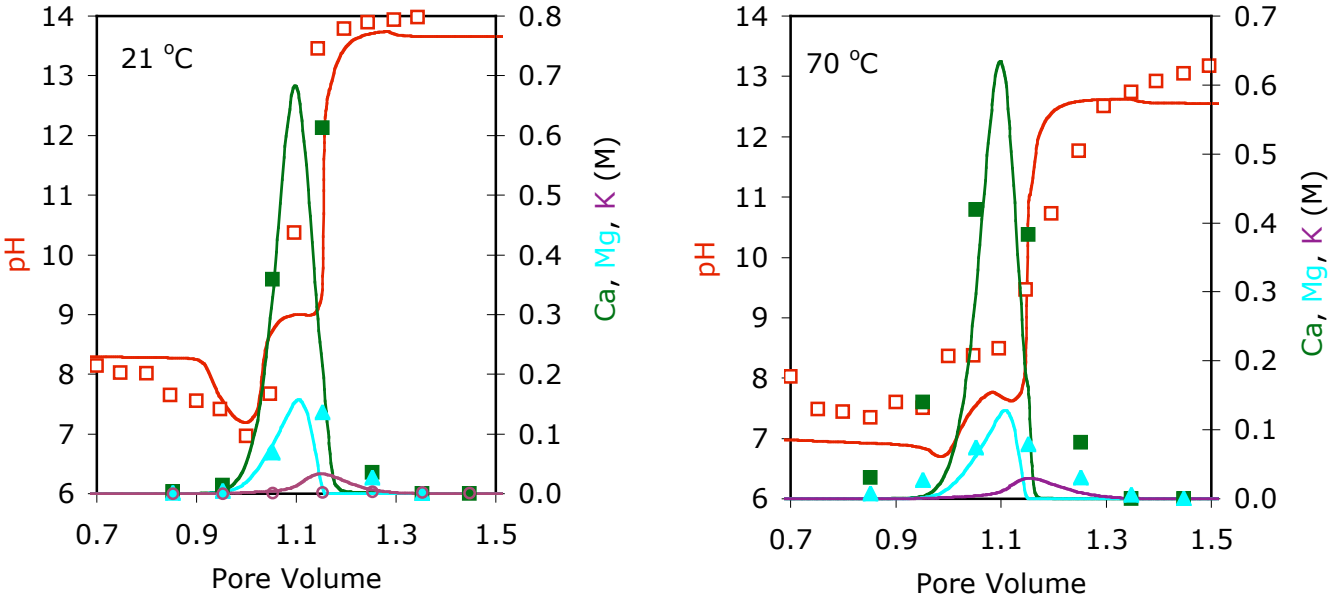

Figure 3

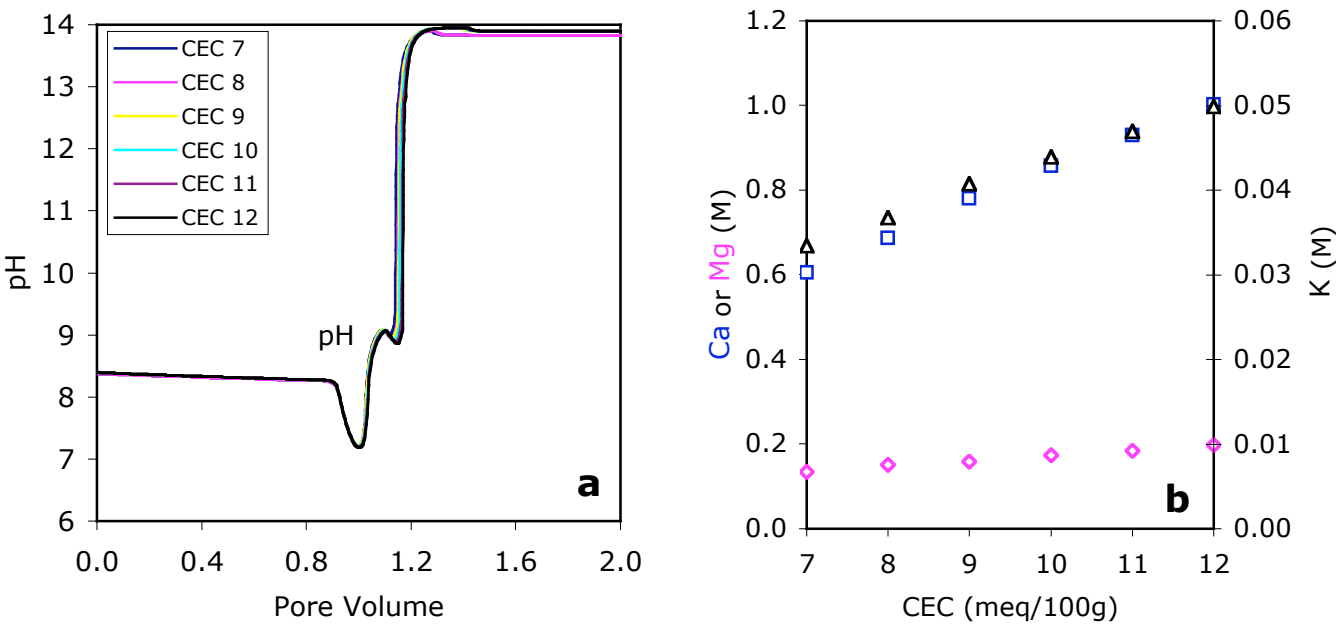

Figure 4

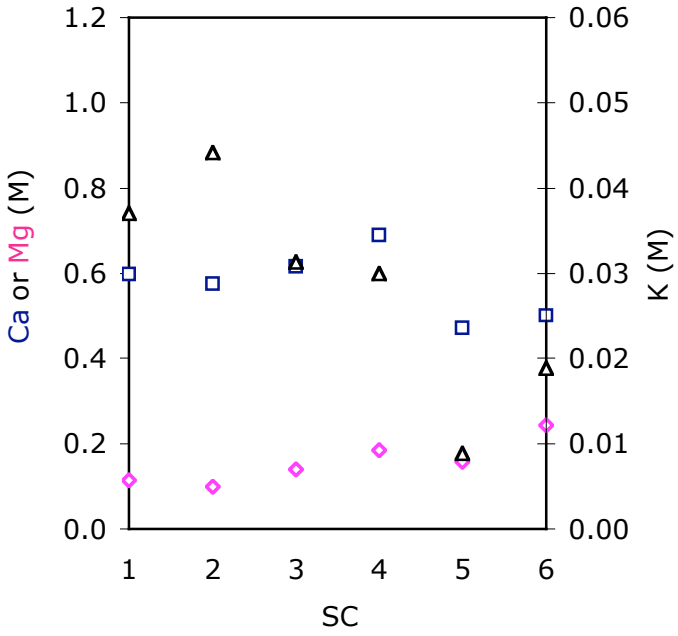

Figure 5

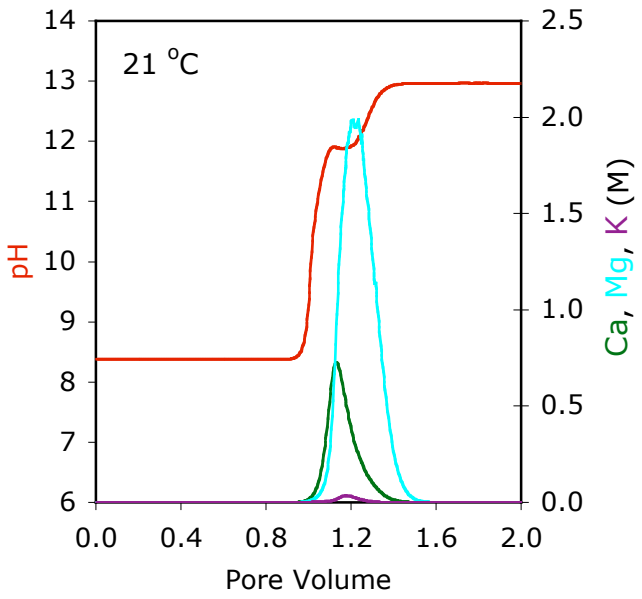

Figure 6

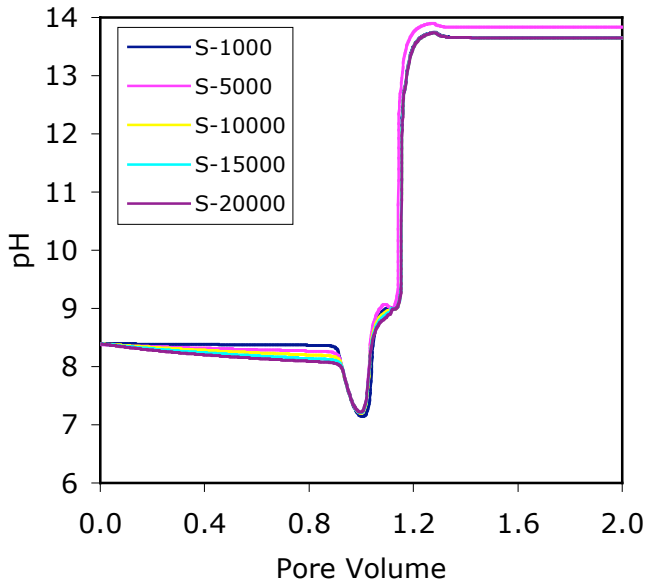

Figure 7

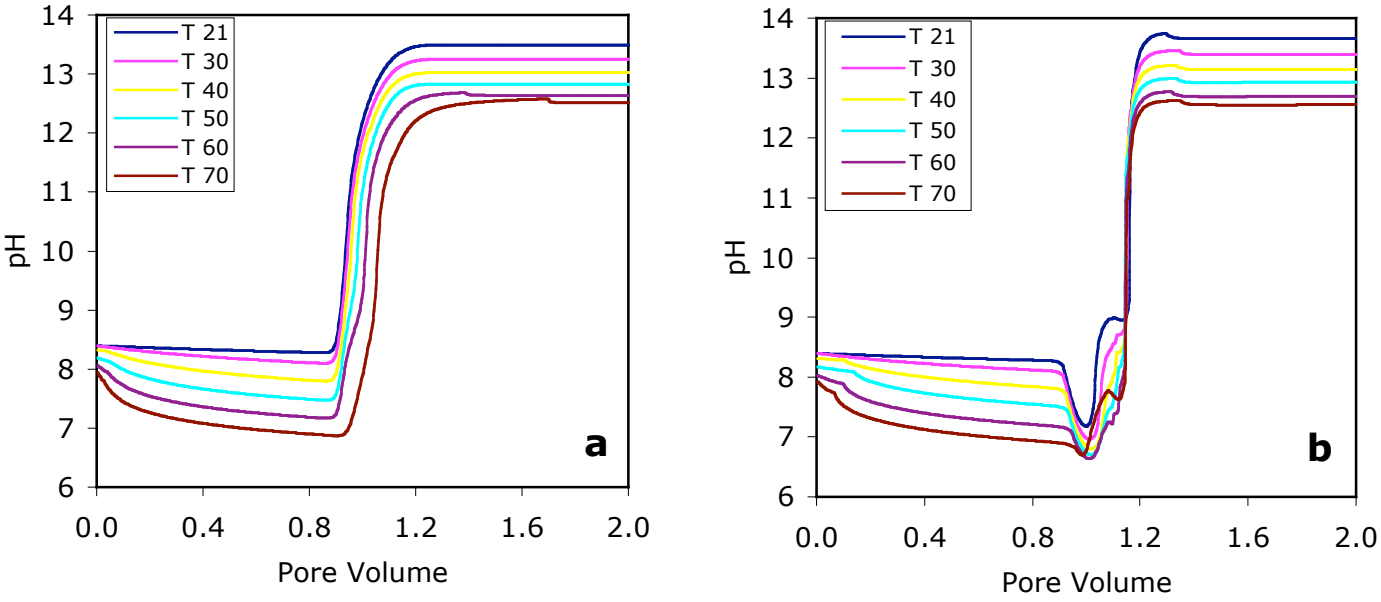

Figure 8

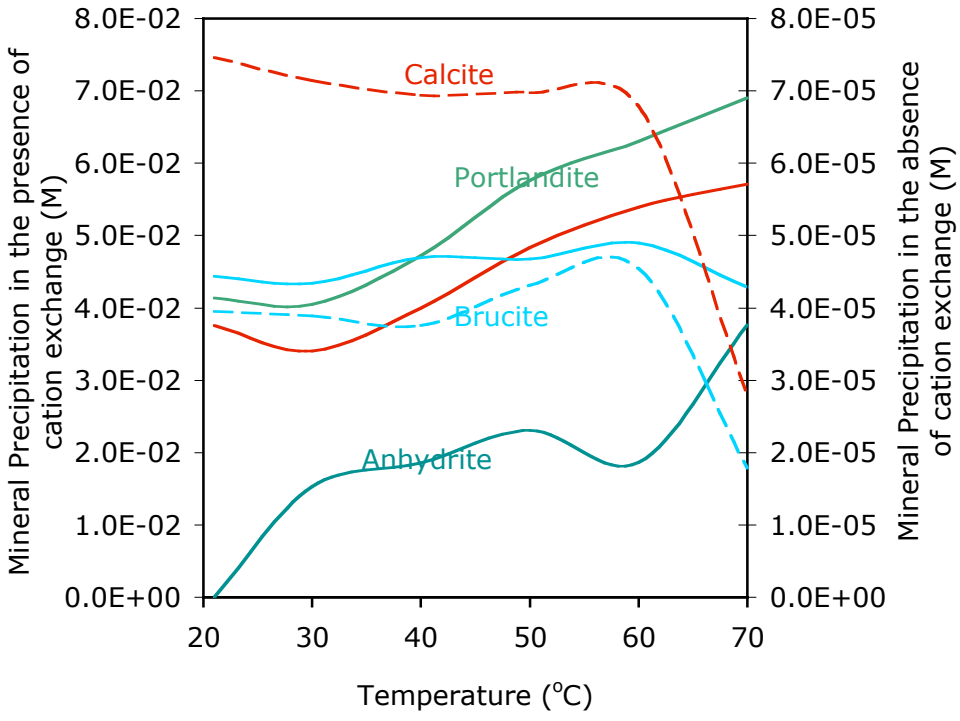

Figure 9

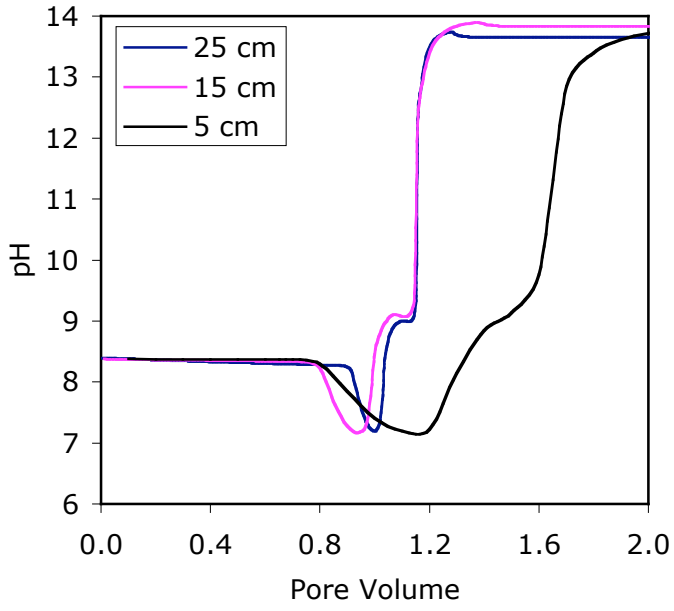

Figure 10